Supplementary Information

Supplementary note 1: Experimental details

Supplementary note 1.1: Coherent population trapping (CPT)

To polarize the nitrogen nuclear spin into $|+1\rangle_N$, the electron spin is first polarized into $|+1\rangle_e$ by the CPT[1] with the red light resonant to $|A_2\rangle$, which is one of the orbital excited states forming a degenerate three level Λ system with the logical qubit bases $|+1\rangle_e$ and $|-1\rangle_e$[1]. The polarization of the $|A_2\rangle$ light defines the bright state $|B\rangle_e$ to be excited into the $|A_2\rangle$, and the dark state $|D\rangle_e$ to remain. For example, the $|+1\rangle_p$ polarized light excites only the bright state $|-1\rangle_e$ into $|A_2\rangle$, which relaxes to the bright or dark states with 50:50 probabilities, so that the logical qubit eventually converges to the dark state $|+1\rangle_e$ by repeating the excitations.

The spin pumping process from $|B\rangle_e$ to $|D\rangle_e$ by the CPT is measured by sweeping the gate delay for the photon counting while irradiating the $|A_2\rangle$ light as shown in Supplementary Figure 1a. The irradiation time in the demonstration is set to 500 ns at a sample power of 500 nW to sufficiently initialize the logical qubit into the dark state. On the other hand, the spin relaxation dynamics into $|0\rangle_e$ is measured by sweeping the irradiation time of the $|A_2\rangle$ light as shown in Supplementary Figure 1b. The population almost completely saturates at around 6.5% of the total population after 500 ns of irradiation.

The Quantum Monte Carlo wavefunction (QMCWF) method[2] is used to simulate the spin pumping and relaxation dynamics. The successful event of the photon absorption is judged every time division ($t_{div} = 1$ ns) by the generated random number in accordance with the double success probability of both optical excitation into $|A_2\rangle$ based on the Jaynes–Cummings model with the Rabi frequency Ω and that of the radiative relaxation from $|A_2\rangle$ as $1 - \exp(-t/\tau)$, where the relaxation time τ is set to 12 ns[3]. The simulations are repeated 10,000 times for every time division to reduce statistical variation. We count the number of absorption events until the electron relaxes into $|D\rangle_e$ or $|0\rangle_e$. We set the probability of relaxation from $|A_2\rangle$ into $|B\rangle_e, |D\rangle_e$ and $|0\rangle_e$ to be respectively $(1-\gamma_0)/2, (1-\gamma_0)/2$ and γ_0. As a result of the simulation using γ_0 and Ω as fitting parameters, we obtained $\Omega = 33$ MHz and $\gamma_0 = 3.19\%$. This result indicates that the probability ratio of the relaxation into $|0\rangle_e$ against $|D\rangle_e$ is $\frac{3.19}{48.41} \times 100 = 6.59\%$, which is consistent with a probability of 6.5% for the experimentally obtained saturated population in $|0\rangle_e$.

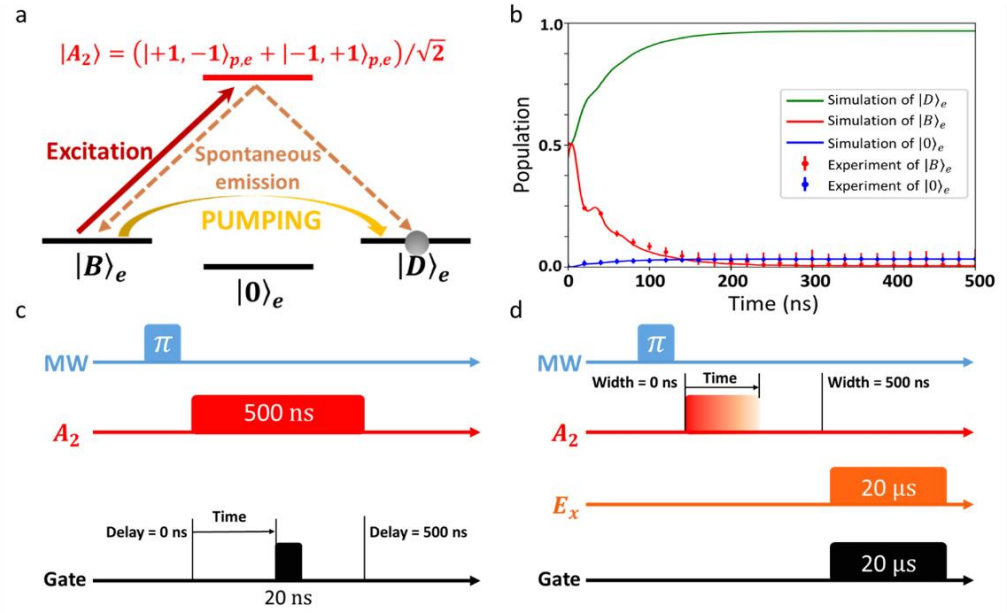

Supplementary Figure 1 | Spin dynamics by CPT. **a**, Schematic level diagram relevant to CPT dynamics. **b**, Time dependence of the spin population during the CPT process under the exposure to $|A_2\rangle$ light. Red and blue dots show respectively the measured populations in the bright state $|B\rangle_e$ and the ancilla state $|0\rangle_e$. Red, blue and green solid lines respectively show the simulated populations in $|B\rangle_e$, $|0\rangle_e$ and the dark state $|D\rangle_e$, which indicate that the population is mainly pumped from $|B\rangle_e$ into $|D\rangle_e$ but partially leaks to $|0\rangle_e$. **c**, Pulse sequence for time dependence measurement of the population in $|B\rangle_e$ measured by the $|A_2\rangle$ emission. **d**, Pulse sequence for time dependence measurement of the population in $|0\rangle_e$ measured by the $|E_x\rangle$ emission. About 6.5% of the population undergoes relaxation to $|0\rangle_e$.

Supplementary note 1.2: Initialization of electron, nitrogen, and carbon nuclear spins

At the beginning of all experiments, we irradiated a green light[4] of 150 μW for 30 μs to initialize the electron spin, the nuclear spin environment and the charge state of the NV center so that we could repeat the experiments under the same conditions (at the left of Supplementary Figure 2). Initialization in experimental sequences of the electron spin into $|0\rangle_e$ is carried out by continuous excitation by the $|A_1\rangle$ light, which has less influence on the carbon nuclear spin[5].

The nitrogen nuclear spin is initialized into $|+1\rangle_N$ by the composite operations, which consist of the electron spin initialization, the CNOT gates between electron and nitrogen, and the CPT process as shown in Supplementary Figure 2. The CPT is performed by continuous excitation with the $|+1\rangle_p$-polarized $|A_2\rangle$ light (500 nW, 500 ns), which polarizes the electron spin into $|+1\rangle_e$. The CNOT gates mutually controlled with the electron and nitrogen are carried out by applying a microwave π pulse (2877 MHz) and a radiowave π pulse (7 MHz) with a frequency tuned to the energy splitting caused by a nuclear quadrupole splitting and the hyperfine coupling. The initialization rate estimated from the ODMR spectrum is 94%, where the error is mainly due to the unintentional relaxation into $|0\rangle_e$ during the CPT process.

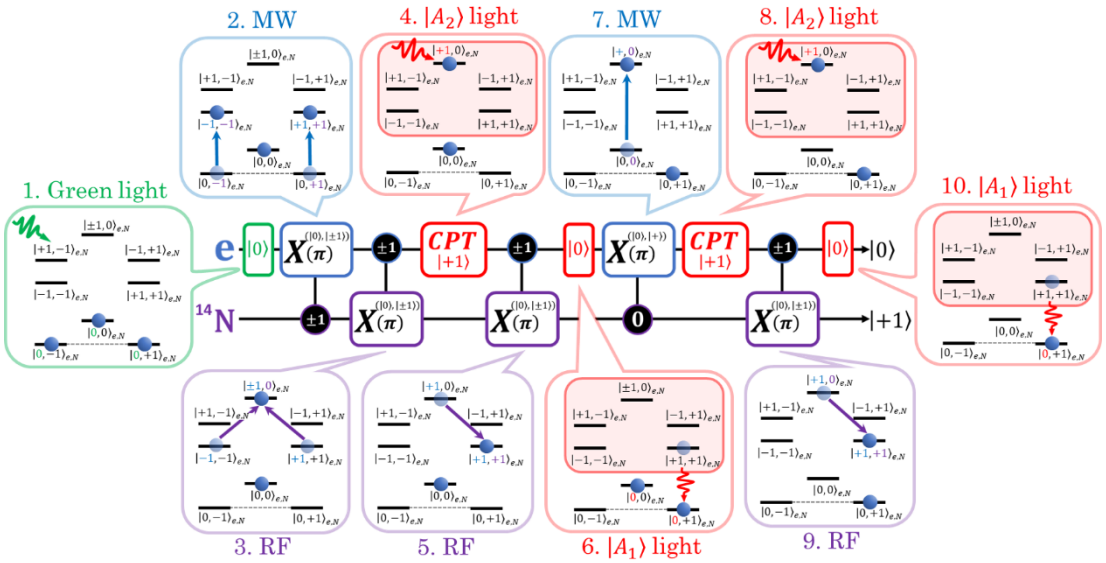

Supplementary Figure 2 | Quantum circuit for nitrogen initialization. The quantum circuit diagram and the level diagram showing the population transitions expected by the quantum gates. We initialize the nitrogen into $|+1\rangle_N$ by performing the SWAP gate between the nitrogen and electron twice together with the CPT process to polarize the electron spin into $|+1\rangle_e$ with the $|A_2\rangle$ light. Gates are defined as $X_{(\pi)}^{(|a\rangle,|b\rangle)} = |a\rangle\langle b| + |b\rangle\langle a| + |d\rangle\langle d|$.

The carbon nuclear spin is initialized into $|\uparrow\rangle_C$ by the SWAP gate consisting of two CNOT gates mutually controlled with the electron and carbon after the initialization of both electron spin and nitrogen nuclear spin as shown in Supplementary Figure 3. The conventional CNOT gates are not possible due to the degeneracy under a zero magnetic field. We therefore utilize the nitrogen as a nanomagnet acting only on the adjacent electron spin by initializing the nitrogen nuclear spin into $|+1\rangle_N$, which lifts the degeneracy of the electron spin while retaining the carbon nuclear spins under a zero magnetic field[6], allowing us to carry out the CNOT gates controlled by the carbon nuclear spin simply by the energy selectivity.

Although we tuned the magnetic field along the quantization axis to zero by monitoring the ODMR spectrum of a single NV center, the magnetic field vertical to the quantization axis can remain. With this transverse magnetic field, the carbon nuclear spin can rotate around X axis even if the electron spin is in $|0\rangle_e$[7]. This enabled the CNOT gate operation on the carbon nuclear spin conditioned by the electron spin by simply waiting for the π rotation[7] (dashed CNOT gate in Supplementary Figure 3). Instead, we used a radiowave resonant to the hyperfine splitting (0.9 MHz) with the electron spin in $|\pm1\rangle_e$ for electron-carbon entanglement generation and readout of the carbon nuclear spin since the rotation axis is controllable.

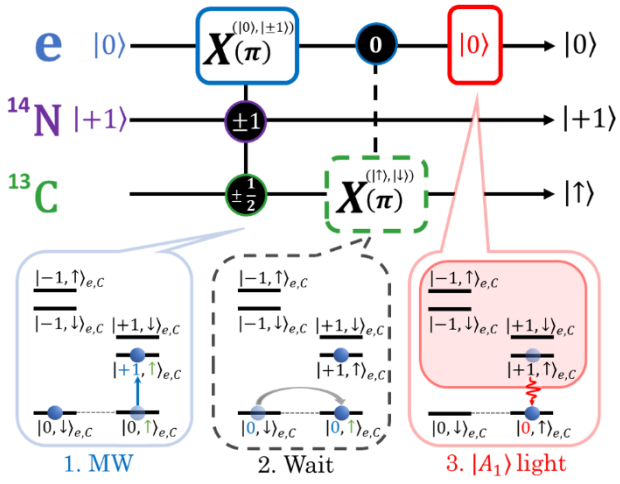

Supplementary Figure 3 | Quantum circuit for carbon initialization. The quantum circuit diagram and the level diagram showing the population transitions expected by the quantum gates. We initialize the carbon into $|\uparrow\rangle_C$ by performing the SWAP gate between the carbon and electron together with the initialization of the electron spin into $|0\rangle_e$ with the $|A_1\rangle$ light.

Supplementary note 1.3: Quantum teleportation-based transfer

The polarization state of the photon is transferred into the carbon nuclear spin state based on the principle of quantum teleportation[8,9,10]. The quantum teleportation scheme consists of the entanglement generation and Bell state measurement mediated by an ancillary quantum media to herald the success of the state transfer.

We generate the electron-carbon entanglement through the following sequence (Supplementary Figure 4a). After the initialization of the nitrogen and carbon nuclear spins, the electron spin is first polarized into $|0\rangle_e$ with the $|A_1\rangle$ light and then flipped into $|+1\rangle_e$ by applying a microwave π pulse to operate the SU(3) Toffoli gate. When the nitrogen and carbon nuclear spins have the same sign, the first microwave π pulse flips the electron spin from $|0\rangle_e$ into $|\pm 1\rangle_e$, which has the same sign as the nuclear spins:

$$\mathrm{MW1} = X_{(\pi)}^{(|0\rangle,|+1\rangle)} \otimes |+1\rangle_N\langle +1| \otimes |\uparrow\rangle_C\langle\uparrow| + X_{(\pi)}^{(|0\rangle,|-1\rangle)} \otimes |-1\rangle_N\langle -1| \otimes |\downarrow\rangle_C\langle\downarrow|. \quad (1)$$

An equal superposition state of the carbon nuclear spin is then prepared by applying an RF π/2 pulse, which operates the Hadamard gate on the carbon. The operation can be written as follows since it changes the sign of a half-*Y* flip of carbon according to the state of the electron spin:

$$\begin{aligned}\mathrm{RF} = {} & |+1\rangle_e\langle +1| \otimes \mathrm{I}_N \otimes Y_{(-\pi/2)}^{(|\uparrow\rangle,|\downarrow\rangle)} + |-1\rangle_e\langle -1| \otimes \mathrm{I}_N \otimes Y_{(+\pi/2)}^{(|\uparrow\rangle,|\downarrow\rangle)} \\ & + |0\rangle_e\langle 0| \otimes \mathrm{I}_N \otimes \mathrm{I}_C.\end{aligned} \quad (2)$$

An electron-carbon entanglement is then prepared by applying two microwave π pulses, which operate two CNOT gates on the electron spin controlled by the nitrogen and carbon nuclear spins, where the microwaves are optimized by GRAPE[11] to fully utilize the frequency selectivity of the electron spin state depending on the carbon nuclear spin state. The operation by the second microwave π pulse is written as:

$$\mathrm{MW2} = X_{(\pi)}^{(|0\rangle,|+1\rangle)} \otimes |+1\rangle_N\langle +1| \otimes \mathrm{I}_C + X_{(\pi)}^{(|0\rangle,|-1\rangle)} \otimes |-1\rangle_N\langle -1| \otimes \mathrm{I}_C. \quad (3)$$

The operation by the third microwave π pulse flips the electron spin from $|0\rangle_e$ into $|\pm 1\rangle_e$, which has the same sign as the carbon nuclear spin when the nitrogen nuclear spin is not in $|0\rangle_N$:

$$\begin{aligned}\mathrm{MW3} = {} & X_{(\pi)}^{(|0\rangle,|+1\rangle)} \otimes (|+1\rangle_N\langle +1| + |-1\rangle_N\langle -1|) \otimes |\uparrow\rangle_C\langle\uparrow| \\ & + X_{(\pi)}^{(|0\rangle,|-1\rangle)} \otimes (|+1\rangle_N\langle +1| + |-1\rangle_N\langle -1|) \otimes |\downarrow\rangle_C\langle\downarrow|,\end{aligned} \quad (4)$$

where the obvious term $\mathrm{I}_e \otimes |0\rangle_N\langle 0| \otimes \mathrm{I}_C$ is omitted for all the above gates since the electron spin and the carbon nuclear spin are not affected when the nitrogen nuclear spin is $|0\rangle_N$.

We then measure the electron-photon state in the Bell basis by using an optical excited state whose spin angular momentum is entangled with the orbital angular momentum, which corresponds to the polarization of the absorbed photon under a zero magnetic field[12]. It is thus possible to perform Bell state measurement between an electron and a photon by observing the absorption of the photon via the optical excited state (Supplementary Figure 4b).

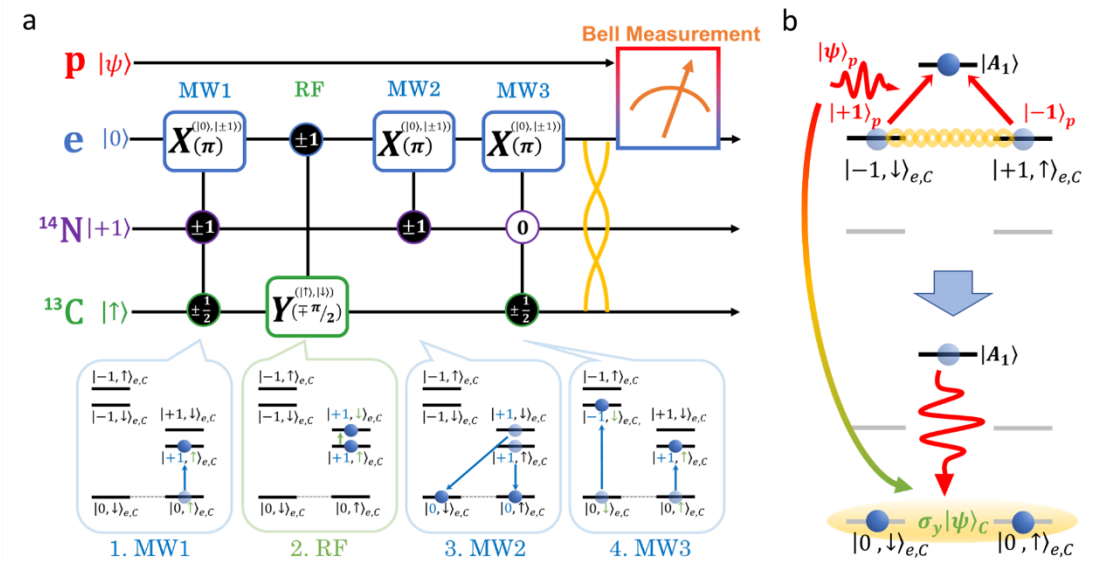

Supplementary Figure 4 | Dynamics of quantum teleportation-based transfer. a, Quantum circuit diagram for the quantum teleportation-based transfer. After the initializations of the electron, nitrogen and carbon, entanglement between the electron and carbon is generated by applying the MW1 and the Hadamard-like gate with the RF followed by the CNOT-like gates with the MW2 and MW3. **b**, The process of the Bell state measurement between the incoming photon and the electron by photon absorption into the $|A_1\rangle$ state. Since $|\Phi^+\rangle_{e,C}$ is generated and then $|A_1\rangle = |\Psi^-\rangle_{p,e}$[12] is measured, the photon polarization state is transferred into the carbon spin state with additional gate operation σ_y.

Supplementary note 1.4: Tomography measurement of carbon nuclear spin

Quantum state tomography measurement[13] is carried out to identify the quantum state of the carbon nuclear spin transferred from the photon. Although the detection of an photon absorption by monitoring an ancillary quantum media $|0\rangle_e$ provides the heralding signal for the success of the transfer[2] (Supplementary Figure 4b), we do not rely on this process to improve the experimental efficiency. Instead, we measure only the successful events by properly designing the readout sequence. By performing the CPT into $|+1\rangle_e$ at the beginning of the readout sequence, the successful events projected on $|0\rangle_e$ remain unchanged, and the failure events projected on either $|\pm1\rangle_e$ are pushed into $|+1\rangle_e$. This

allows us to use the $\{|0\rangle_e/|-1\rangle_e\}$ space for heralding the success of the transfer (Supplementary Figure 5). After all, by performing quantum state tomography measurement of the carbon nuclear spin with a sequence that does not read out the case where the state of the electron spin is $|+1\rangle_e$, only the successful events are read out. In the actual entanglement generation process, the population remaining in $|\pm1\rangle_e$ without entangled is not detectable and thus degrades the transfer fidelity, while population remaining in $|0\rangle_e$ is detectable and thus does not degrade the transfer fidelity.

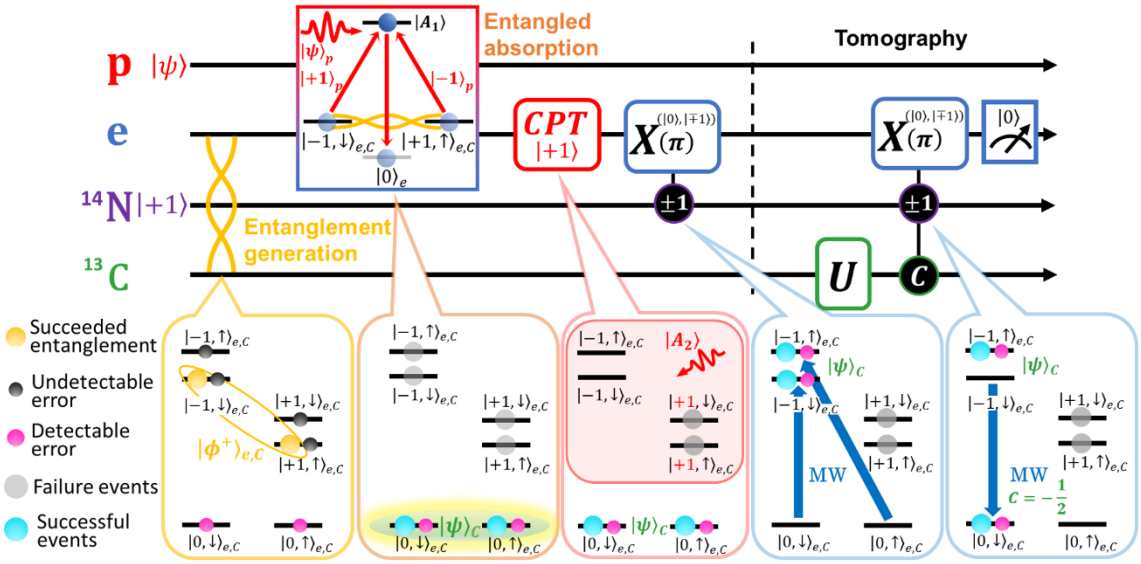

Supplementary Figure 5 | Quantum circuit for tomography measurement. The sequences of the quantum state tomography measurement realized by selecting U and C as shown in Supplementary Table 1 on the six measurement bases. Failure events are not measured by performing CPT to $|+1\rangle_e$. The detectable error is excluded by performing the four types of measurements in Supplementary Figure 6.

For the measurement of each of the six basis polarization states ($|+\rangle_C$, $|-\rangle_C$, $|+i\rangle_C$, $|-i\rangle_C$, $|\uparrow\rangle_C$, $|\downarrow\rangle_C$), we set the unitary gates U and control qubit states C for the quantum circuit in Supplementary Figure 5 as shown in Supplementary Table 1. The Bloch vector components of the nuclear spin state are defined as visibilities V_A $(A = X, Y, Z)$ obtained by projection amplitudes on six mutually-biased bases $P_B(B = |+\rangle_C, |-\rangle_C, |+i\rangle_C, |-i\rangle_C, |\uparrow\rangle_C, |\downarrow\rangle_C)$ as follows.

$$V_X = \frac{P_{|+\rangle_C} - P_{|-\rangle_C}}{P_{|+\rangle_C} + P_{|-\rangle_C}}, V_Y = \frac{P_{|+i\rangle_C} - P_{|-i\rangle_C}}{P_{|+i\rangle_C} + P_{|-i\rangle_C}}, V_Z = \frac{P_{|\uparrow\rangle_C} - P_{|\downarrow\rangle_C}}{P_{|\uparrow\rangle_C} + P_{|\downarrow\rangle_C}}. \quad (5)$$

Projection	$\|+\rangle_C$	$\|-\rangle_C$	$\|+i\rangle_C$	$\|-i\rangle_C$	$\|\uparrow\rangle_C$	$\|\downarrow\rangle_C$
$\boldsymbol{U}$	$\boldsymbol{Y}^{(\|\uparrow\rangle,\|\downarrow\rangle)}_{(+\pi/2)}$	$\boldsymbol{Y}^{(\|\uparrow\rangle,\|\downarrow\rangle)}_{(-\pi/2)}$	$\boldsymbol{X}^{(\|\uparrow\rangle,\|\downarrow\rangle)}_{(-\pi/2)}$	$\boldsymbol{X}^{(\|\uparrow\rangle,\|\downarrow\rangle)}_{(+\pi/2)}$	$\boldsymbol{I}$	$\boldsymbol{I}$
$\boldsymbol{C}$	$+\frac{1}{2}$	$+\frac{1}{2}$	$+\frac{1}{2}$	$+\frac{1}{2}$	$+\frac{1}{2}$	$-\frac{1}{2}$

Supplementary Table 1 | Quantum circuit design for tomography measurement. The sequence of the tomography measurement shown in Supplementary Figure 5 depends on the measurement basis by setting U and C as in this table.

We performed the projective measurements to estimate the projected components along the measurement basis only on the successful event of transfer. The population P of each basis was obtained from the photon detection counts $I_{A_{1_b},CX_b}\,(b = on, off)$ obtained from the four kinds of measurements (Supplementary Figure 6) for each of the six bases by the following equation:

$$P = \frac{I_{A_{1_{on}},CX_{on}} - I_{A_{1_{off}},CX_{on}}}{I_{A_{1_{on}},CX_{off}} - I_{A_{1_{off}},CX_{off}}}\,, \tag{6}$$

where the subscripts of the photon detection counts I indicate the experimental conditions. $A_{1_{on}}/A_{1_{off}}$ indicates whether or not the NV is irradiated with the $|A_1\rangle$ light for transfer, and CX_{on}/CX_{off} indicates whether or not two CNOT gates in Figure 5 are applied. The population just before readout in each case is shown in Supplementary Figure 6.

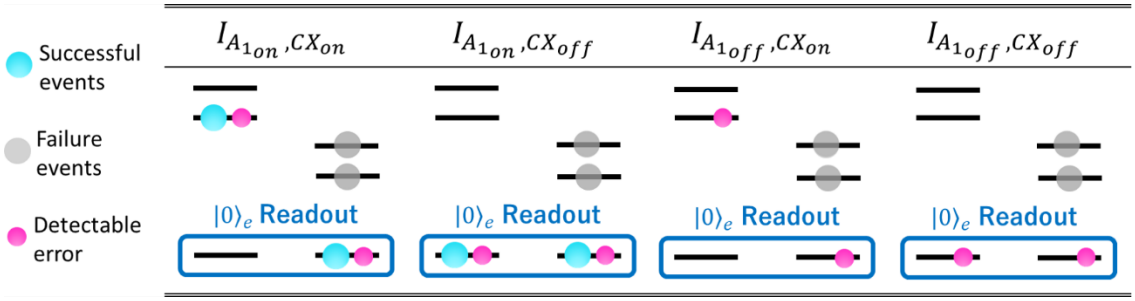

Supplementary Figure 6 | Four types of measurements for post selection. The population arrangement obtained by switching on and off the $|A_1\rangle$ light and last CNOT gate in the quantum circuit shown in Supplementary Figure 5 are shown. The projection on the measurement basis for the successful events of transfer is estimated by normalizing the emission counts for the four kinds experiments based on Eq. (6).

Our demonstration aims to read out the carbon nuclear spin state transferred from a photon based on the quantum teleportation principle. We performed preliminary experiments to evaluate the measurement fidelities of the quantum tomography measurement (Supplementary Figure 7). We prepared three basis states $(|+\rangle_C, |+i\rangle_C, |\uparrow\rangle_C)$ of the carbon nuclear spin and projected them into six complete basis states $(|+\rangle_C,\ |-\rangle_C,\ |+i\rangle_C,\ |-i\rangle_C,\ |\uparrow\rangle_C,\ |\downarrow\rangle_C)$ (Supplementary Figure 7a). The carbon nuclear spin states are prepared by applying the SU(3) *X* gate and the *R* gate as shown in Supplementary Figures 7a and 7b after initializing into $|\uparrow\rangle_C$. The readout quantum circuit is designed as shown in Supplementary Table 1 in the same manner as that for the quantum teleportation-based transfer. Supplementary Figures 7c and 7d indicate that the measurement bases are at least orthogonal to each other.

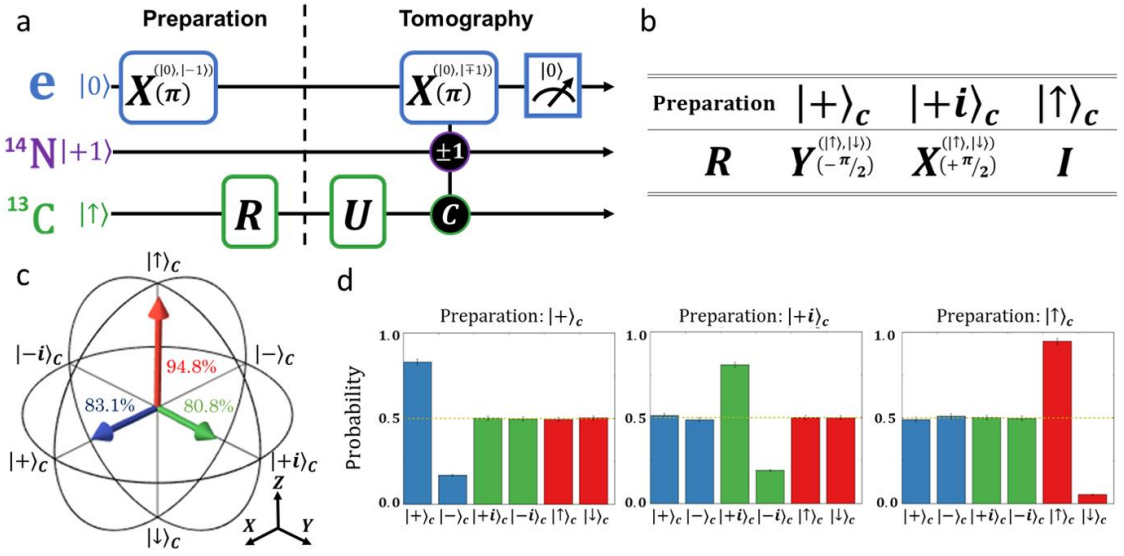

Supplementary Figure 7 | Tomography measurement of carbon. a, Quantum circuit for the carbon nuclear spin state tomography measurement. The tomography portion is the same as the tomography measurement circuit in Supplementary Figure 5. Three basis states $|+\rangle_C, |+i\rangle_C, |\uparrow\rangle_C$ are prepared by designing the unitary gate *R* according to the table shown in **b**. **b**, Design table of the quantum circuits. Set the unitary gate *R* according to the state you want to prepare with the preparation part of **a**. **c**, **d**, Results of the tomography measurement experiment. In **c**, we draw on the Bloch sphere, and in **d**, we show measurement results for 6 bases, $(|+\rangle_C,\ |-\rangle_C,\ |+i\rangle_C,\ |-i\rangle_C,\ |\uparrow\rangle_C,\ |\downarrow\rangle_C)$, for each of 3 quantum states, $|+\rangle_C, |+i\rangle_C, |\uparrow\rangle_C$. Error bars in **c** and **d** are within 2%.

Supplementary note 2: Factor analysis of transfer fidelity degradation

Supplementary note 2.1: Incomplete initialization of spins

Incomplete nuclear spin initialization results in degradation of the transfer fidelity through the degradation of the entanglement. The transfer fidelities as functions of the initialization errors for the nitrogen nuclear spin p_N into $|-1\rangle_N$ and the carbon nuclear spin p_C into $|\downarrow\rangle_C$ are calculated, where the initialization error for the nitrogen nuclear spin into $|0\rangle_N$ is not considered since it is excluded by the post selection. The initial state of the composite system consisting of the electron spin, nitrogen nuclear spin, and carbon nuclear spin is described as

$$\begin{aligned}(1-p_N)(1-p_C)|0,+1,\uparrow\rangle\langle 0,+1,\uparrow| \;+\; (1-p_N)p_C|0,+1,\downarrow\rangle\langle 0,+1,\downarrow| \\ +\; p_N(1-p_C)|0,-1,\uparrow\rangle\langle 0,-1,\uparrow| \;+\; p_Np_C|0,-1,\downarrow\rangle\langle 0,-1,\downarrow|,\end{aligned} \tag{7}$$

where the spin states of the electron, nitrogen, and carbon are represented as $|m_e\rangle\otimes|m_N\rangle\otimes|m_C\rangle = |m_e, m_N, m_C\rangle$. When the entangling gates shown in Supplementary Figure 4a are applied, we get the following state:

$$\begin{aligned}(1-p_N)(1-p_C)|+1\rangle_N\langle +1|\otimes|\Phi^+\rangle_{e,C}\langle\Phi^+| \;+\; (1-p_N)p_C|+1,+1,\downarrow\rangle\langle +1,+1,\downarrow| \\ +\; p_N(1-p_C)|-1,-1,\uparrow\rangle\langle -1,-1,\uparrow| \;+\; p_Np_C|-1\rangle_N\langle -1|\otimes|\Phi^+\rangle_{e,C}\langle\Phi^+|.\end{aligned} \tag{8}$$

Supplementary Figure S.8 shows the simulated transfer fidelity obtained by projecting the final state as Eq. (8) into the entangled state between the photon and electron, which is written as $|\Psi^-\rangle_{p,e}$. That the fidelity for the circularly polarized light (Supplementary Figures 8b and 8c) is lower than the fidelity for the linearly polarized light (Supplementary Figure 8a) indicates that the initialization error contributes significantly to the amplitude ratio rather than the phase coherence of the entanglement. Equation (8) also indicates that classical states such as $|+1,+1,\downarrow\rangle, |-1,-1,\uparrow\rangle$ are generated due to the initialization error. The averaged degradation of the fidelity of the quantum teleportation-based transfer with the initialization error of 6% for the nitrogen nuclear spin $|-1\rangle_N$ and 10% for the carbon nuclear spin $|\downarrow\rangle_C$ is estimated from the ODMR spectrum to be 10.5%. In addition, the simulated transfer fidelity of the $|-1\rangle_p$ is lower than that of the $|+1\rangle_p$, which is consistent with the experimental result that the transfer fidelity of the $|+1\rangle_C$ corresponding to $|-1\rangle_p$ is lower than that of the $|-1\rangle_C$ corresponding to $|+1\rangle_p$, as shown in Figures 3c and 3d.

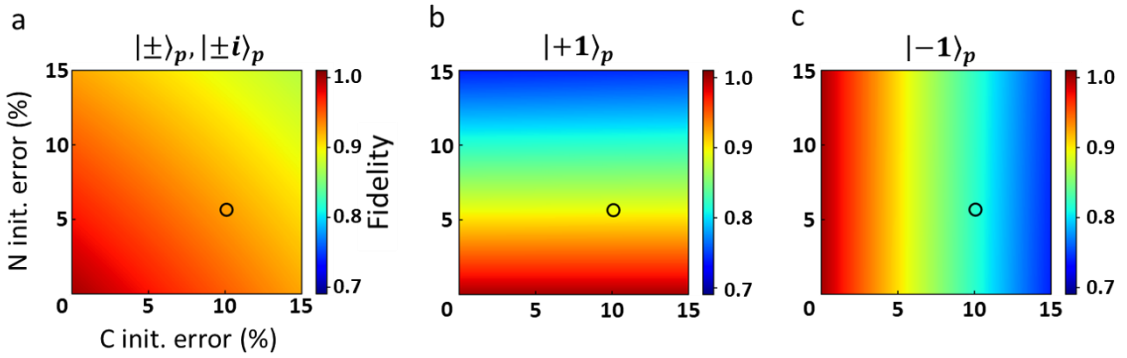

Supplementary Figure 8 | Relationship between the initialization errors of nuclear spins and transfer fidelity. Simulated dependence of the transfer fidelity on the initialization errors for the carbon and nitrogen nuclear spins for the photon polarizations **a**, $|+\rangle_p$, $|-\rangle_p$, $|+i\rangle_p$, $|-i\rangle_p$, **b**, $|+1\rangle_p$, and **c**, $|-1\rangle_p$. The solid circles represent the ranges of the initialization errors for this demonstration.

Supplementary note 2.2: Mixing of orbital excited states due to crystal strain

The orbital excited states of the electron are mixed by the crystal strain, which is represented by the strain Hamiltonian[12]. In this demonstration, the orbital excited state $|A_1\rangle(|\Psi^-\rangle_{p,e})$ used for Bell state measurement of the photon and electron is mixed with the $|E_1\rangle(|\Phi^-\rangle_{p,e})$ and $|E_2\rangle(|\Phi^+\rangle_{p,e})$ by the crystal strain, and thus the projection on the mixed state is different from the ideal entangled state. In this situation, the state of the carbon nuclear spin transferred from the photon is distorted in the Bloch sphere. Therefore, it differs from the ideal transfer state to carbon nuclear spin, resulting in fidelity degradation as shown in Supplementary Figure 9. This effect can also be confirmed from the fact that the experimental result in Figure 3c seems to be biased toward $|+\rangle_C$. The comparison of the PLE measurement with the simulation indicates that the strength of the crystal strain at the NV center used in the demonstration is 1.8 GHz, where the fidelity degradation due to crystal strain is 2% on average. The effect of crystal strain on the polarization can be simulated by analyzing the strain Hamiltonian[6]. Although the direction of the crystal strain represented by e_x and e_y is not fully identified, the experimental results shown in Figure 3c suggest that the transferred state is distorted toward the direction of $|+\rangle_C$. This implies that the crystal strain is likely to be e_x, which does not lower the fidelity for the $|\pm\rangle_p$ polarized light and drops the fidelities for the $|\pm i\rangle_p$ and $|\pm 1\rangle_p$ polarized lights as shown in Supplementary Figure 9. The teleportation-based transfer can be adopted to the crystal strain by calibrating the polarization with the perfect knowledge of the strain vector.

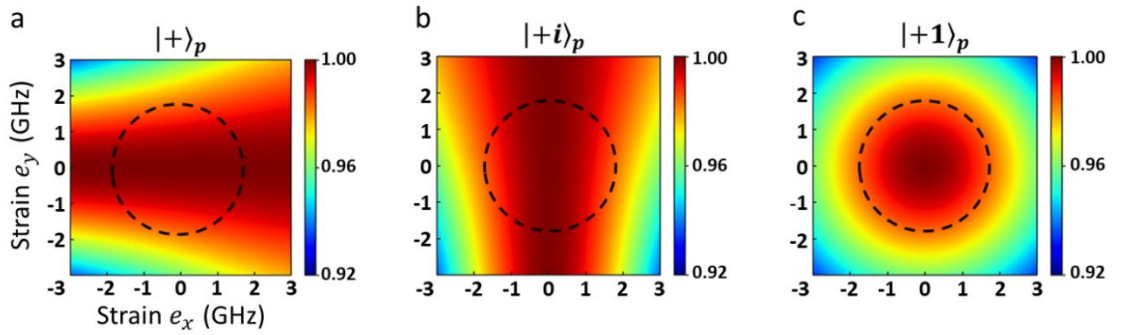

Supplementary Figure 9 | Relationship between the crystal strain and transfer fidelity. Simulated dependence of the transfer fidelity on the two vector components of the crystal strain for the photon polarizations as in **a**, **b**, and **c**. Results for $|-\rangle_p$ and $|-i\rangle_p$ are obtained by inverting the y axis of the results of $|+\rangle_p$ and the x axis of the results of $|+i\rangle_p$, respectively. Dashed circles represent the ranges of the crystal strain components for this demonstration.

Supplementary note 2.3: Phase rotation during the Bell state measurement

We developed a technique to polarize nitrogen nuclear spin to $|+1\rangle_N$ and utilize it as a nanomagnet for only electron spin, thereby successfully controlling carbon nuclear spin under a zero magnetic field. While the electron spin whose degeneracy was eliminated by this method allows improved operability, a splitting of about 4 MHz, which is twice the hyperfine interaction between the nitrogen nuclear spin and electron spin, is introduced by nitrogen nuclear spin between the levels of $|+1,\uparrow\rangle_{e,C}$ and $|-1,\downarrow\rangle_{e,C}$ of the electron-carbon entanglement $|\Phi^+\rangle_{e,C}$ (Supplementary Figure 10a). Due to this splitting, the relative phase of $|\Phi^+\rangle_{e,C}$ rotates at a frequency of about 4 MHz. The irradiation time of $|A_1\rangle$ light is set to 20 ns with 200 nW, and photon polarization and electron spin are measured in the Bell basis by photon absorption[1] after the dynamics of the optical Rabi oscillation to reach $|A_1\rangle$ and relaxation to $|0\rangle$ during the irradiation time. However, there is a time width at the time when the Bell state measurement actually takes place, and the phase of the Bell state changes until that time, resulting in degradation of the transfer fidelity (Supplementary Figure 10b). As can be seen from Supplementary Figure 10, the fidelity degradation deteriorates the phase component, which is noticeable in the transfer of the state with phase information. One of the solutions to this problem is to polarize nitrogen nuclear spin into $|+1\rangle_N$ to make the electron spin non-degenerate until the entanglement generation, where the nitrogen nuclear spin is flipped back to $|0\rangle_N$ to degenerate the electron again. The method well utilizes the merits of non-degeneracy and degeneracy. However, since the nitrogen nuclear spin states $|\pm1\rangle_N$ are degenerate, a

circularly polarized radiowave is required to create or annihilate only the $|+1\rangle_N$ from/to $|0\rangle_N$. The polarized microwave also allows us to selectively operate the $|\pm1\rangle_e$ states without lifting the degeneracy of the electron spin using nitrogen nuclear spin as a nanomagnet, resulting in higher fidelity.

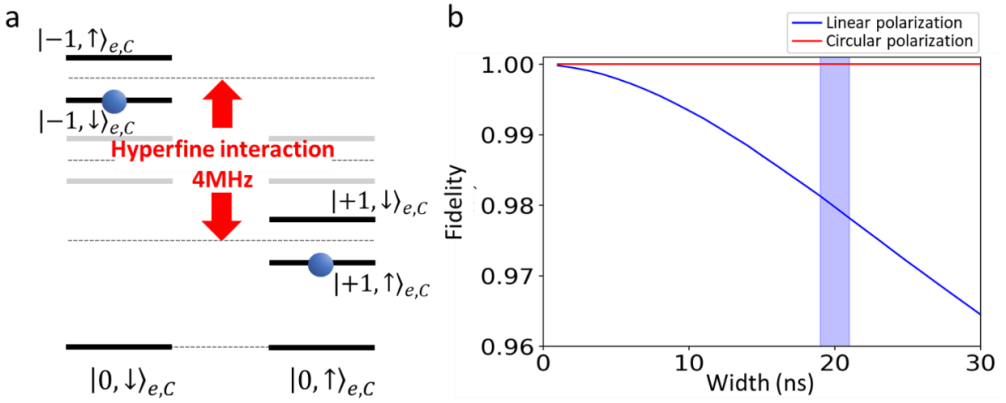

Supplementary Figure 10 | Relationship between the energy difference of entanglement levels and transfer fidelity. a, An electron-carbon partial system in which the degeneracy was lifted. By polarizing nitrogen nuclear spin to $|+1\rangle_N$, 4 MHz splitting occurs between the electron-carbon entanglement levels $|\Phi^+\rangle_{e,C}$, due to the nitrogen-electron hyperfine interaction, which causes phase rotation. **b**, Fidelity degradation in the presence of energy splitting. This graph was obtained by statistically processing the fidelity at the time when absorption occurred for every 1 ns of $|A_1\rangle$ irradiation time. Since phase rotation occurs between entanglement levels, the transfer fidelity does not degrade when $|+1\rangle_p$ or $|-1\rangle_p$ is transferred, and it drops when $|+\rangle_p, |-\rangle_p, |+i\rangle_p$, or $|-i\rangle_p$ is transferred.

Supplementary note 3: Validity check of single-photon absorption

An optical pulse (power: 200 nW; width: 20 ns) is used for this demonstration instead of a single photon. However, the probability of absorbing a photon more than once is low, and a one-photon experiment can be performed with a good approximation, since the relaxation from $|A_1\rangle$ takes 12 ns[3] and photon absorption occurs stochastically. In order to show this, simulation by QMCWF was performed under the following conditions (Supplementary Figure 11). The state of the electron spin after relaxation from $|A_1\rangle$ is either the bright state $|B\rangle_e$ or the dark state $|D\rangle_e$, both of which are in the $\{|+1\rangle_e/|-1\rangle_e\}$ space, or $|0\rangle_e$; the relaxation probabilities of the three states are 30%, 30%, and 40%, respectively[2]. The π pulse time was calculated from the fitting result in 1.1.CPT (power: 500 nW; π pulse time: 15 ns). The calculations were performed without subsequent absorption once the electron relaxed to $|0\rangle_e$. We also set up a condition in which 4 MHz splitting between $|\pm1\rangle_e$ occurs due to the hyperfine interaction of the nitrogen nuclear spin $|+1\rangle_N$. We simulated 10,000 times at each point (1 ns) to reduce statistical variations, and the results are shown in Supplementary Figure 11. The results show that the probability of one-photon absorption is 97.5% over the photon absorption events for 20 ns of irradiation.

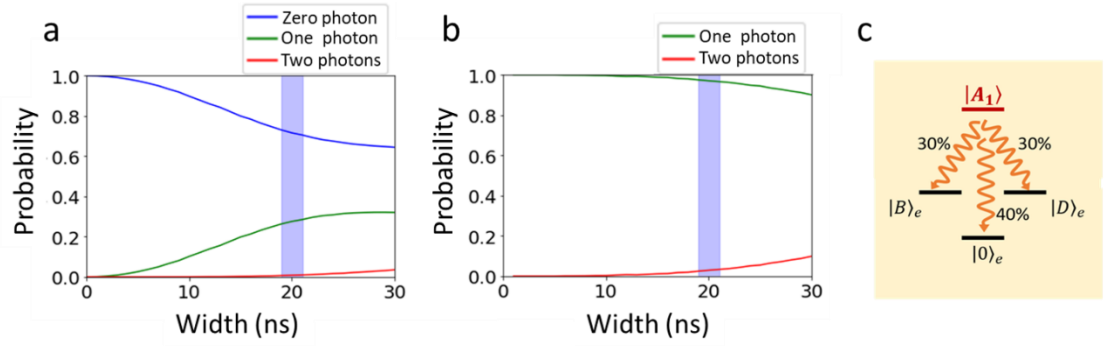

Supplementary Figure 11 | Probability of two-photon absorption depending on the $|A_1\rangle$ irradiation time. a, The probabilities that relaxation to $|0\rangle_e$ never happens (blue), that it occurs by the first absorption (green), and that it occurs by the second absorption (red) are obtained from the QMCWF simulation. **b**, Conditional probability in the case of relaxation to $|0\rangle_e$. In this experiment, the probability of this two-photon absorption leads to a deterioration of transfer fidelity. **c**, Conditions for the simulation of the two-photon absorption. In addition, since the nitrogen nuclear spin is polarized to $|+1\rangle_N$, a split of 4 MHz occurs between $|-1\rangle_e$ and $|+1\rangle_e$.

Supplementary References

1. Kosaka, H. & Niikura, N. Entangled absorption of a single photon with a single spin in diamond. *Phys. Rev. Lett.* **114,** 053603 (2015).
2. Yang, S. *et al.* High fidelity transfer and storage of photon states in a single nuclear spin. *Nat. Photon.* **10,** 507–511 (2016).
3. Goldman, M. L. *et al.* Phonon-induced population dynamics and intersystem crossing in nitrogen-vacancy centers. *Phys. Rev. Lett.* **114,** 145502 (2015).
4. Doherty, M. W. *et al.* The nitrogen-vacancy colour centre in diamond. *Phys. Rep.* **528,** 1–45 (2013).
5. Robledo, L. *et al.* High-fidelity projective read-out of a solid-state spin quantum register. *Nature* **477,** 574–578 (2011).
6. Sekiguchi, Y., Niikura, N., Kuroiwa, R., Kano, H. & Kosaka, H. Optical holonomic single quantum gates with a geometric spin under a zero field. *Nat. Photon.* **11,** 209–214 (2017).
7. Rao, K. R. K. & Suter, D. Characterization of hyperfine interaction between an NV electron spin and a first-shell C 13 nuclear spin in diamond. *Phys. Rev. B* **94,** 060101 (2016).
8. Nielsen, M. A. & Chuang, I. *Quantum computation and quantum information*. (Cambridge University Press, 2000).
9. Bennett, C. H. *et al.* Teleporting an Unknown Quantum State via Dual Classical and Einstein-Podolsky-Rosen Channels. *Phys. Rev. Lett.* **70,** 1895–1899 (1993).
10. Bouwmeester, D. *et al.* Experimental quantum teleportation. *Nature* **390,** 575–579 (1997).
11. Khaneja, N. K. *et al.* Optimal Control of Coupled Spin Dynamics : Design of NMR Pulse Sequences by Gradient Ascent Algorithms. *J. Magn. Reson.* **172,** 296–305 (2005).
12. Maze, J. R. *et al.* Properties of nitrogen-vacancy centers in diamond: The group theoretic approach. *New J. Phys.* **13,** 025025 (2011).
13. Kosaka, H. *et al.* Spin state tomography of optically injected electrons in a semiconductor. *Nature* **457,** 702–705 (2009).